SUPPORTING INFORMATION

Nanoscale-Phase-Separated Pd-Rh Boxes Synthesized via Metal Migration: An Archetype for Studying Lattice Strain and Composition Effects in Electrocatalysis

Brian T. Sneed,[†,‡] Casey N. Brodsky,[†,‡] Chun-Hong Kuo,[‡] Leo K. Lamontagne,[‡] Ying Jiang,[§] Yong Wang,[§] Franklin (Feng) Tao,[∞] Weixin Huang,[∞] and Chia-Kuang Tsung*[,‡]

*To whom correspondence should be addressed. E-mail: frank.tsung@bc.edu

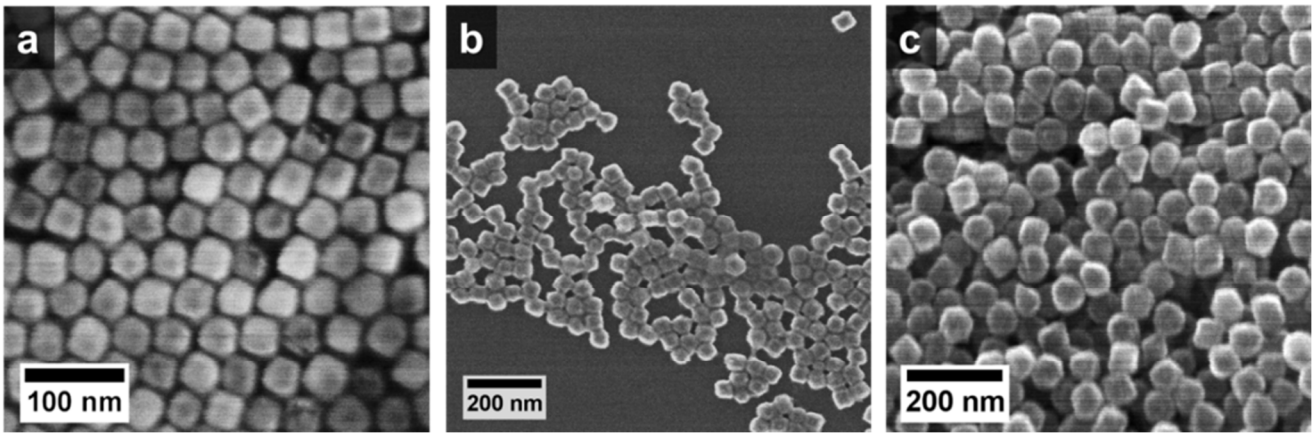

Figure S1. SEM images of Pd-Rh NBs in (a) and Rh cubic NFWs in (b). SEM images of Rh octahedral NFWs are given in (c).

Figure S1(a-c) shows SEM images of the Pd-Rh NBs and Rh NFWs. The dark contrast in the center of the particles is due to the hollow cavities in the structures.

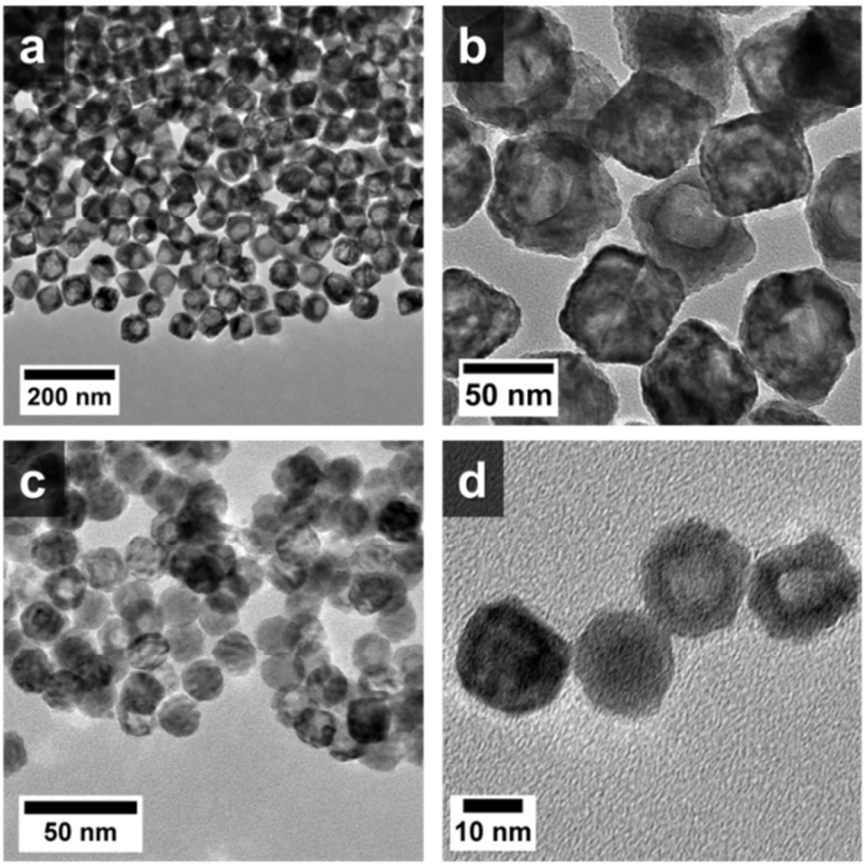

Figure S2. TEM images of (a,b) Pd-Rh nanooctahedra and (c,d) Pd-Rh nanocuboctahedra synthesized by the same method.

Figure S2 shows how the Pd-Rh NB synthesis could be applied to different particle morphologies and sizes. In Figure S2(a,b) ~60 nm Pd-Rh octahedra, and S2(c,d) alloy ~15 nm cuboctahedra were synthesized by following the same route as for the ~30 nm cubic nanostructures. The appearance is not as uniform in these samples as for the NBs, however, we believe the concentration of Rh in the overgrowth in the core-shell formation could be the reason and could be tuned to provide a more uniform batch of particles. However, since we found previously that the cubic structures were more active than the octahedra in electrocatalysis experiments, we did not pursue further optimization or assessment of their catalytic activity.

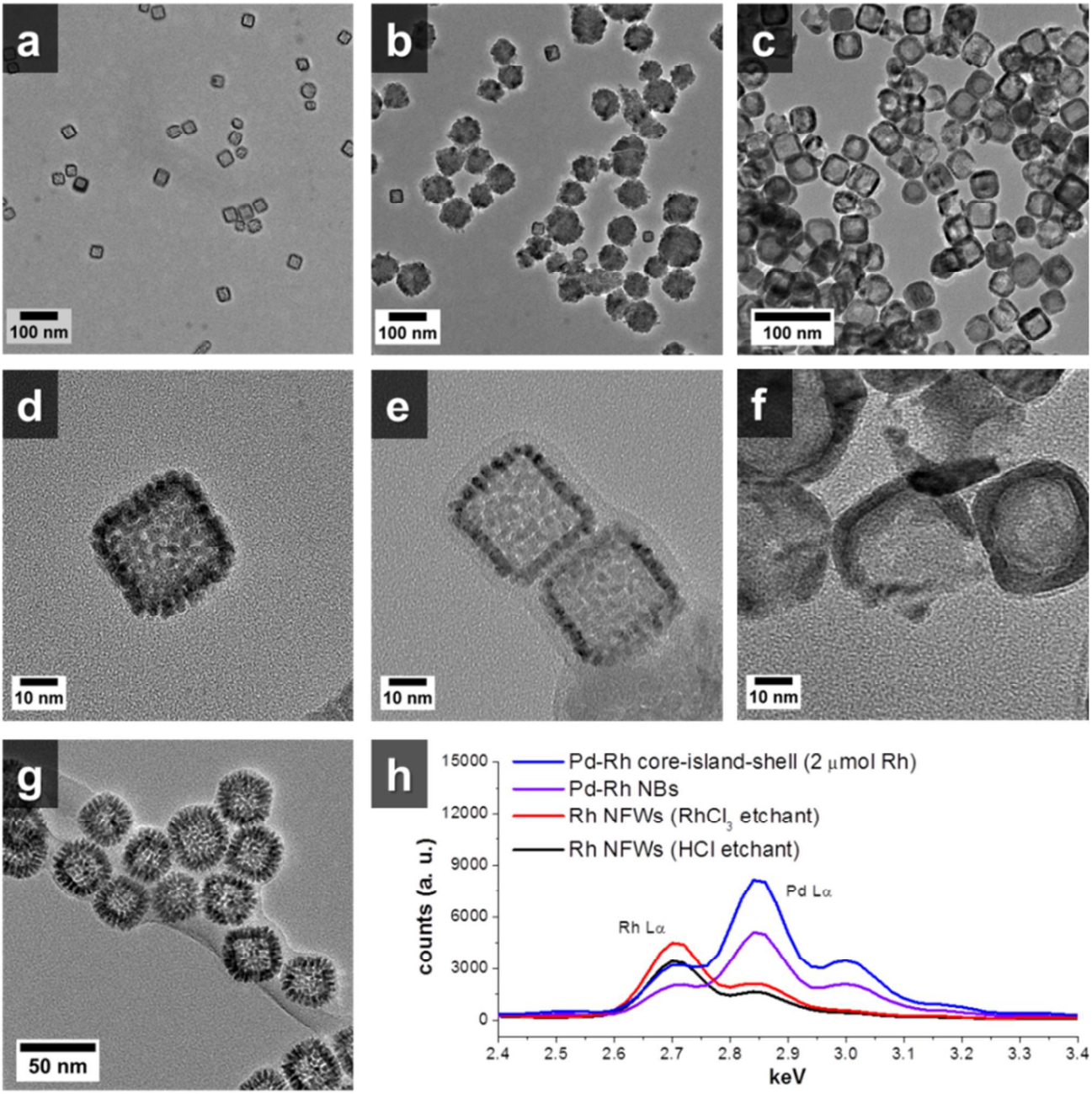

Figure S3. TEM/EDX data for control experiments elucidating the mechanism. In (a,d) are TEM images of particles from rinsed solutions of Pd-Rh NBs treated for 24 hours with $RhCl_3$ added. In (b,e) are images of NBs treated with HCl/$FeCl_3$ as the etchant. In (c,f) are TEM images where the HCl/$FeCl_3$ is added to the original reaction solution prior to the hydrothermal treatment of the synthesis of NBs. In (g) is an image of Rh NFWs generated from addition of dilute HCl to core-shell NPs. EDX spectra are shown in (h) of core-island-shell NPs, NBs, and NFWs generated from intermediate amounts of Rh (2.0 μmol $RhCl_3$) in the growth step and different etchants (for the etching of NPs, 0.500 mL of either 0.01 M HCl, 0.01 M $RhCl_3$, or 0.01 M $FeCl_3$/HCl was added).

Figure S3(a-g) shows TEM images of particles from control experiments that confirm the migration and etching mechanisms. Pd is selectively removed from the Pd-Rh nanostructures when HCl, $FeCl_3$, or $RhCl_3$ is added as the etchant to rinsed nanoparticle solutions. However, when etchant is added to the original reaction solution prior to the formation of Pd-Rh NBs (shown in Figure S3-(c,f)), the Pd oxidative removal does not occur completely because of the initially reducing environment. Figure S3(h) gives EDX elemental analysis to show the particle composition. It can be observed that the relative ratio of Pd:Rh in both core-shell and NB nanostructures remains the same after the migration to form NBs. This indicates that little Pd is lost during the migration step. Whether etched by dilute acids or metal ions, the Pd L-lines are not observed in the spectra for Rh NFWs. It is known that Pd dissolves to some extent in aqueous HCl solutions above 100°C, while Rh does not, so it is not unreasonable to see the result with dilute HCl here since the reaction temperature is held at 110°C for over 24 hours. Note in S3(b) that the large particles are likely iron oxide and formed from the instability of $FeCl_3$ in these conditions.

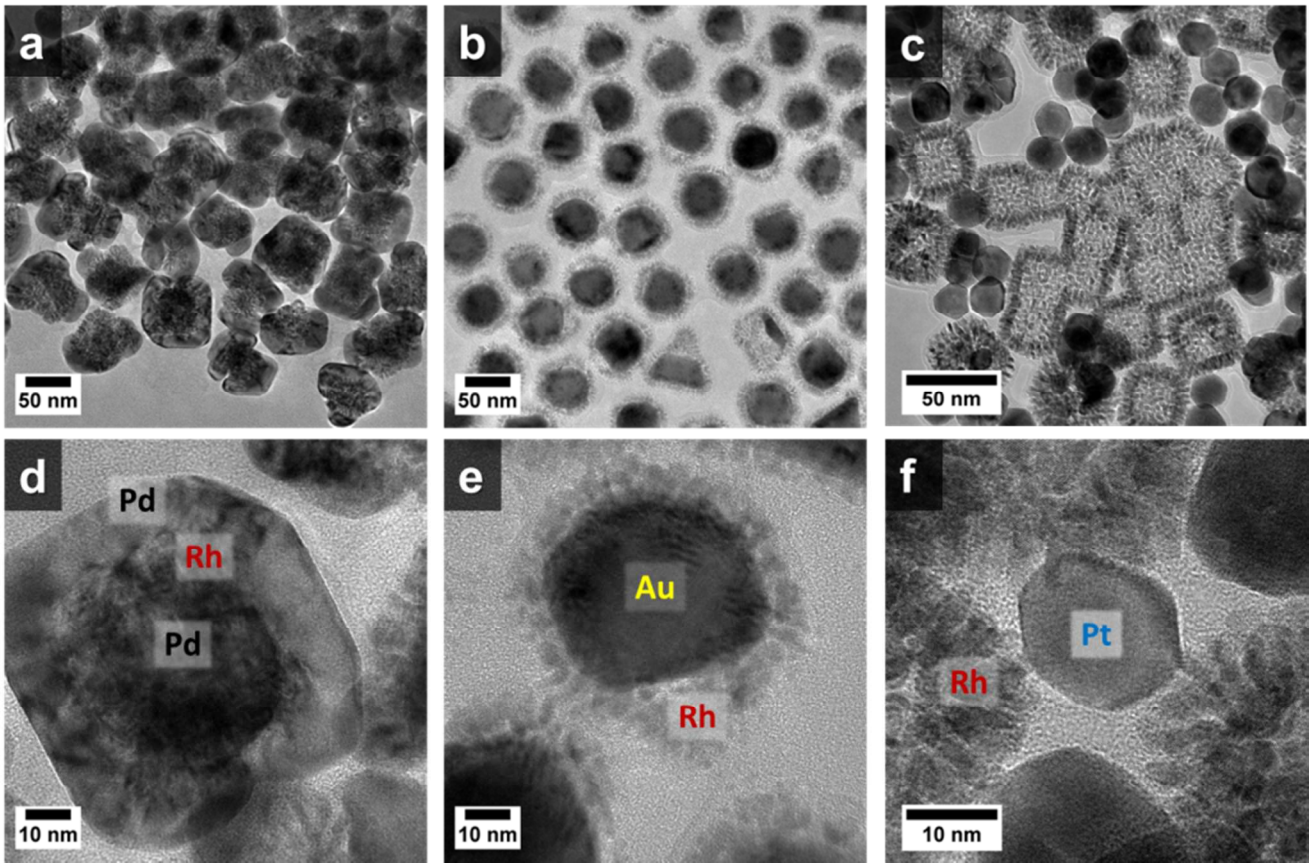

Figure S4. TEM images of control experiments using different metals. In (a,d) are Pd-Rh core-island-shell nanoparticles with over-growth of a layer of Pd. In (b,e) are Au-Rh nanoparticles from the extended treatment in oxidative conditions, and (c,f) contains TEM images of Pd-Rh core-island-shell nanoparticles under prolonged treatment with H_2PtCl_6 (Pt precursor) added to the solution.

Figure S4(a-f) shows the effects of Pt, Au, and additional Pd on the particles. Firstly, in S4(a,d) it is shown that Pd could be reduced overtop the Rh islands. The image in S4(d) shows a particle where epitaxial growth of Pd results in a cubic multi-layered structure. Secondly, etching treatment was carried out on Au-Rh nanoparticles shown in TEM images in S4(b,e) confirming Au was more resilient to the etching treatment than Pd. Finally, addition of Pt precursor to the core-shell Pd-Rh NPs before the extended treatment caused the Pd in the structure to be galvanically replaced by Pt to form Pt NPs. The removal of Pd is apparent in the Rh NFWs from S4(c,f). This is important in displaying Rh's kinetic stability over Pd. Despite Rh having a lower potential for reduction than both Pd and Pt, Pt ions have no effect on the Rh structure, and so there was no indication of galvanic replacement for Rh. Pd was galvanically removed from structure which resulted in Pt nuclei being reduced in solution.

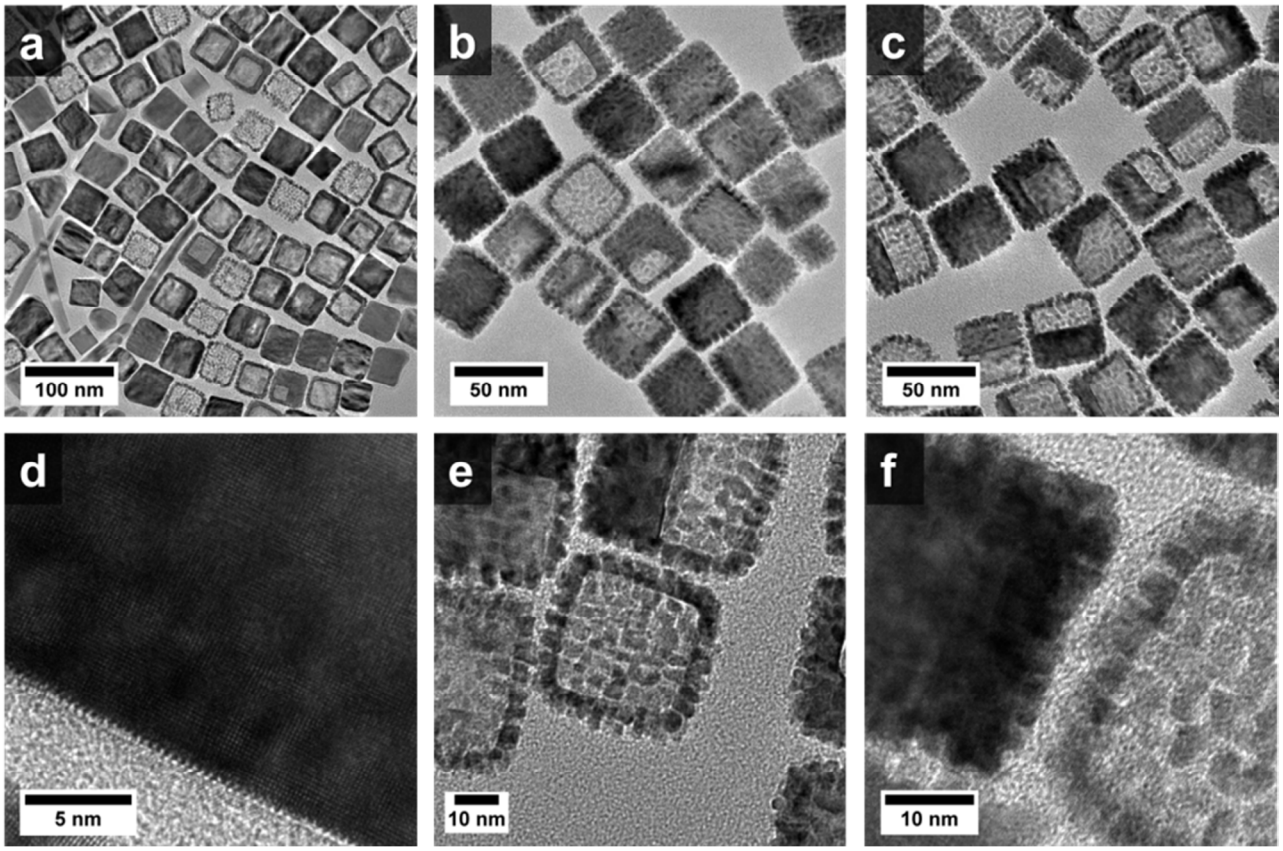

Figure S5. TEM images of experiments investigating the role of reducing agent and halide ion in the prolonged heating treatment to form Pd-Rh NBs, and Rh NFWs. Core-island-shell particles were rinsed and redispersed in CTAB solution directly after their synthesis. Then ascorbic acid, bromide ions, or iodide ions were added to the solution before the extended heating treatment. In (a,d) are NP solutions with ascorbic acid added, (b,e) are NP solutions where bromide ions added, and S5(c,f) are images of particles where iodide ions were added to the solutions.

Figure S5(a-f) shows TEM results of experiments to investigate the role of other components in the synthesis of Pd-Rh NBs and Rh NFWs. Etching was observed with ~50% of the particles in all samples, showing the addition of etchant is necessary to completely etch the Pd in particles. Oxidative etching with halides could remove the Pd from the structures by in the formation of Pd^{2+} complexes. The extended heating without the originally reducing environment helps also to etch the particles. In the case of the addition of reducing agent in S5(a,d), less etching of Pd was observed, as well as intra- and inter-particle Pd migration. This is evidenced by Pd-Rh cubic particles with cores intact and filling of the Rh island framework by Pd to form core-alloy shell particles. The excess reducing agent suppresses oxidation in this way, and the formation of NBs as well as filled NBs could be expected. It is interesting to point out that only the conditions and products of the original overgrowth reaction solution were able to serve to generate highly uniform Pd-Rh NBs (without the intermediate or byproduct structures).

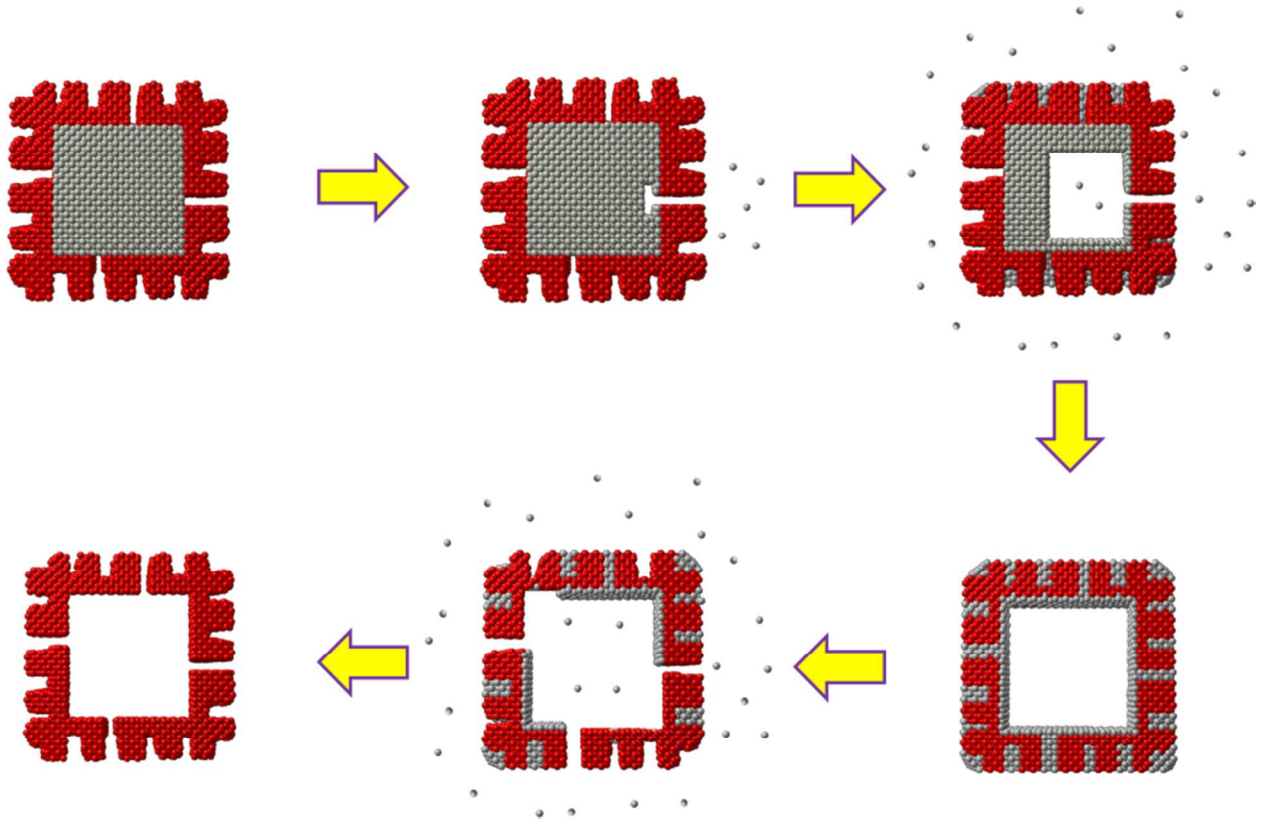

Scheme S1. Scheme showing the proposed migration and etching of Pd from Pd-Rh core-island shell cubes to form Pd-Rh NBs and Rh cubic NFWs.

Scheme S1 shows crystal models depicting the migration and etching of Pd atoms from the Pd-Rh core-island-shell substrate precursor nanostructure. The migration is facilitated by halide ions (bromide and iodide from the overgrowth) and excess reducing agent, and is selective to Pd because of Rh's higher stability. When the environment is oxidative by addition of acid or metal ions and treatment at high temperatures, the Pd will dissolve and this leaves the intact Rh NFW behind.

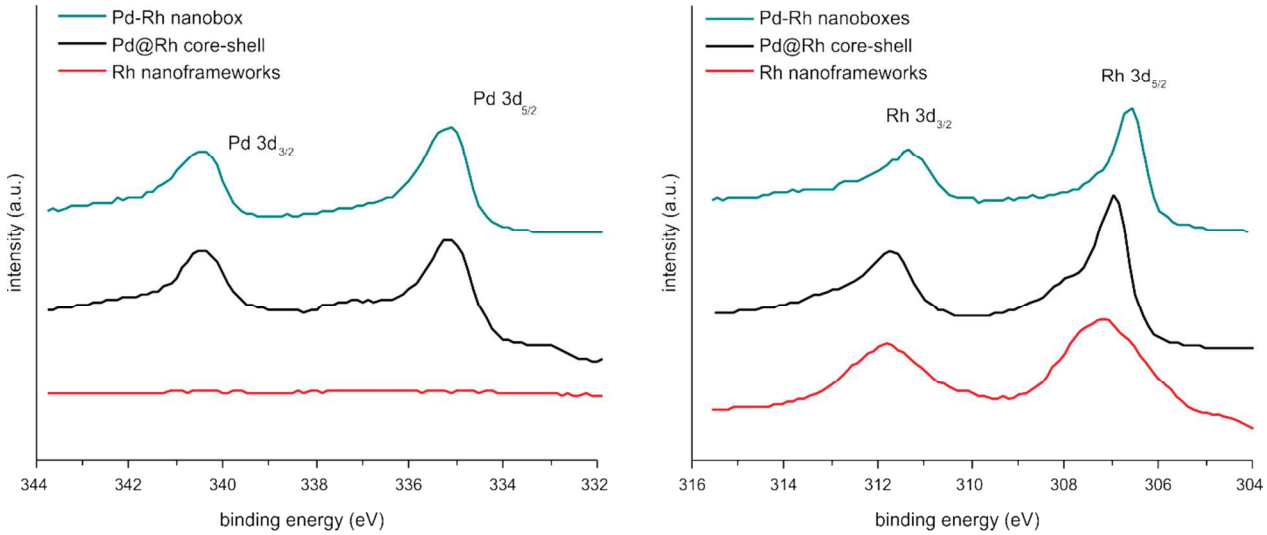

Figure S6. X-ray photoelectron spectra for the three Rh-containing nanostructures showing the shift in the 3d binding energy.

X-ray photoelectron spectroscopy (XPS) of the three types of nanoparticles with Rh surfaces is given in Figure S6. The binding energies of Pd and Rh 3d show a shift for the bimetallic particles compared to the Rh nanoframeworks. This could be a result of compressive and expansive strain on the Pd and Rh lattices, respectively. Other works have connected core-level shifts in strained Pd and Cu nanoparticles to a shift in the d-band center (references 59 and 60 in the main text) of the metal and improved electrocatalysis. In another example, strain in bimetallic nanoparticles (Pd layers deposited on Cu substrates) results in a down-shift of Pd 3d binding energy, and this was directly correlated with a shift-away of the d-band center of the catalyst from the Fermi level of pure Pd.[1] This contributed to the higher activity of the strained catalysts in formic acid electrooxidation.

(1) Hu, S.; Scudiero, L.; Ha, S. *Electrochimica Acta* **2012**, *83*, 354.

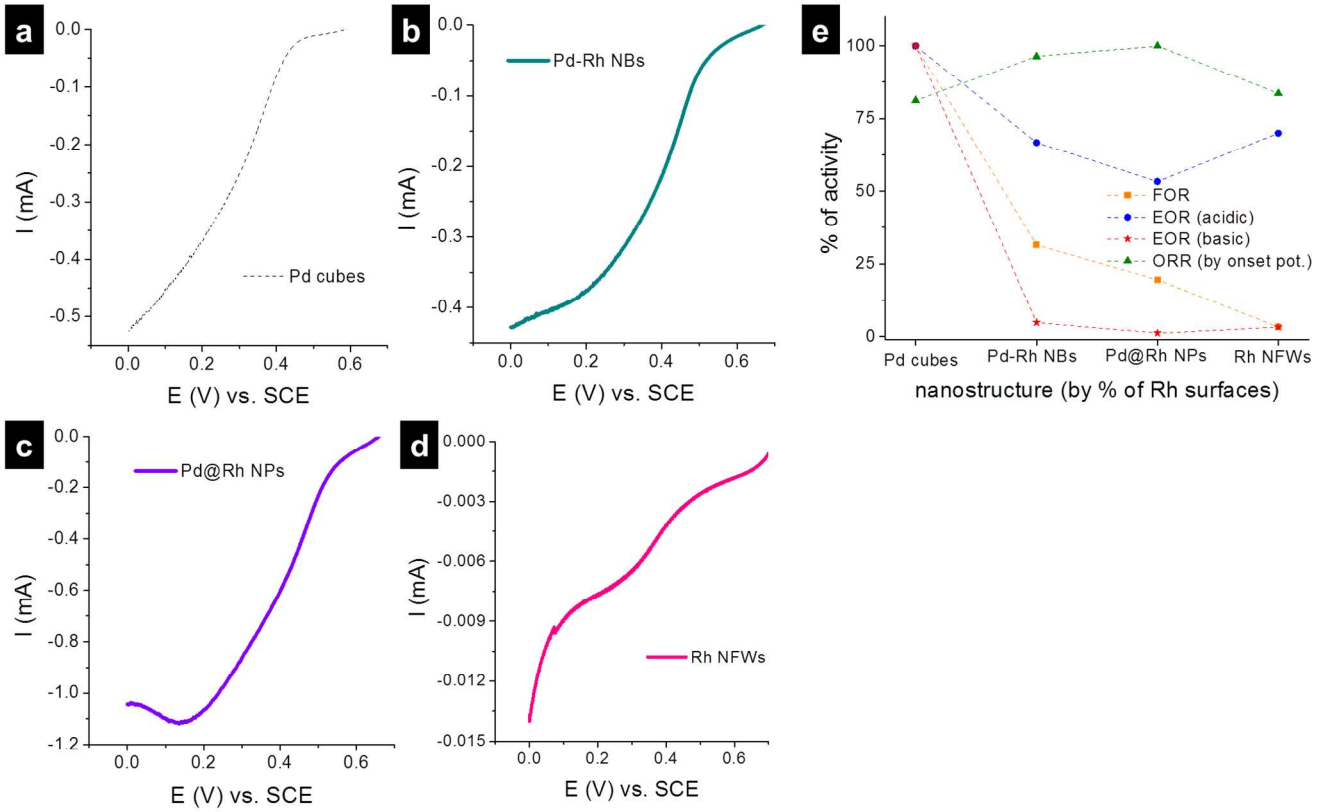

Figure S7. Potential vs. voltage curves for the oxygen reduction reaction catalyzed by Pd-Rh nanoparticles: (a) Pd nanocubes (b) Pd-Rh NBs, (c) Pd@Rh NPs, and (d) Rh nanoframeworks. An activity plot in (e) shows the relative activity by current density for the different reactions and nanoparticle catalysts.

Figure S7(a-e) gives ORR curves and a summary of each of the nanocatalyst structure types for the electrocatalytic reactions performed. FOR and alkaline EOR exhibit increasing activity for increasing Pd composition and ORR exhibits a volcano curve with core-shell NPs exhibiting the highest activity and both Pd-Rh NBs and Rh NFWs outperforming the Pd nanocubes. We attribute their higher onset potentials to strain in the structures.

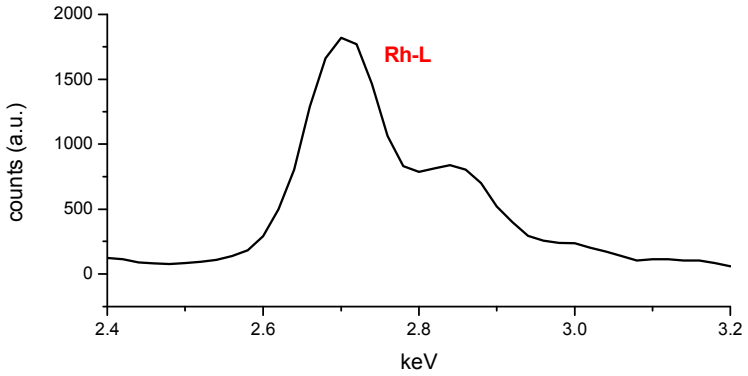

Element	*Line*	*k factor*	*Absorbtion corrn.*	*Weight%*	*Weight% sigma*	*Atomic%*
Rh	L_SERIES	1.249	1	30.34	2.13	9.06
Pd	L_SERIES	1.267	1	-0.49	0.62	-0.14

Figure S8. EDX spectrum for Au-Rh yolk-shell nanoparticles focused on the region for Rh and Pd L-lines. A table giving the quantitative metal percentages is shown below the spectrum.

There is a near zero (negative) count for Pd signal shown in Figure S8 from EDX of the area containing yolk-shell nanostructures.